

Linking Overturning, Recirculation, and Melt in Glacial Fjords

Ken X. Zhao¹, Andrew L. Stewart¹, and James C. McWilliams¹

¹Department of Atmospheric and Oceanic Sciences, University of California, Los Angeles, 405 Hilgard Ave., Los Angeles, CA 90095-1565.

Key Points:

- Simulations show face-wide glacial melt dominates the total melt due to its concentration at deeper depths vs. discharge plume-driven melt.
- Glacial melt in fjords is primarily driven by recirculation at depth for most fjord properties, which is in turn driven by overturning.
- Face-wide glacial melt drives a significant warm-water overturning and recirculation at depth, leading to a melt-circulation feedback.

Abstract

Fjord circulation modulates the connection between marine-terminating glaciers and the ocean currents offshore. These fjords exhibit both overturning and horizontal recirculations, which are driven by water mass transformation at the head of the fjord via subglacial discharge plumes and distributed meltwater plumes. However, little is known about the interaction between the 3D fjord circulation and glacial melt and how relevant fjord properties influence them. In this study, high-resolution numerical simulations of idealized glacial fjords demonstrate that recirculation strength controls melt, which feeds back on overturning and recirculation. The overturning circulation strength is well predicted by existed plume models for face-wide melt and subglacial discharge, while relationships between the overturning, recirculation, and melt rate are well predicted by vorticity balance, reduced-order melt parameterizations, and empirical scaling arguments. These theories allow improved predictions of fjord overturning, recirculation, and glacial melt by taking intrafjord dynamics into account.

Plain Language Summary

Glacial fjords are long, narrow, and deep inlets that connect glaciers to the open ocean. These glacial fjords exist around the margins of Greenland, West Antarctica, Patagonia, Alaska, and other regions, and collectively contribute a significant source of ice discharge into the ocean. Over the past two decades, tidewater glaciers in Greenland have accelerated, which can lead to sea level rise, and there is growing evidence that this acceleration is caused by deep warm water currents that flow into the fjords from the open ocean. These warm water currents have the potential to melt the submarine sides of the tidewater glaciers, causing them to retreat over time. The dynamics of this delivery of warm water to the glacier face, particularly its interaction with fjord circulation, are presently poorly understood. In this study, we use high-resolution, process-oriented simulations to understand the currents within these fjords, how they vary with different fjord characteristics, and how they lead to different rates of submarine melting of the glacier face. We find that the submarine glacial melt can cause feedbacks by amplifying the strength of the ocean currents, which further increase glacial melt. These results are an important step towards understanding a critical process that may help us improve sea level rise predictions.

1 Introduction

Outflowing of marine-terminating glaciers at the margins of the Greenland Ice Sheet and Antarctic Ice Sheet has accelerated in recent years (van den Broeke et al., 2016). For the Greenland Ice Sheet, a major cause of the accelerated melting is postulated to be the warming of deep ocean currents that come into contact with the termini of tidewater glaciers (Wood et al., 2018; Cowton et al., 2018; P. R. Holland et al., 2008; Straneo & Heimbach, 2013).

Submarine melt at marine-terminating glaciers drives glacial retreat and also amplifies iceberg calving depending on the properties of the glacier and fjord (Slater et al., 2021; Wood et al., 2021; Morlighem et al., 2016; Chauché et al., 2014; Fried et al., 2018; Rignot et al., 2015; Wagner et al., 2016). The submarine melt rate consists of ambient face-wide melt and discharge plume-driven melt (Straneo & Cenedese, 2015; Jackson et al., 2019). Although subglacial discharge plumes have the potential to drive a melt rate of more than a meter per day in the glacial area near the plume (equivalent to a volumetric melt of $\mathcal{O}(10^4)$ to $\mathcal{O}(10^5)$ m^3/day , assuming a fjord width of 5 km), it only occupies a small fraction of the glacial face (Cowton et al., 2015; Slater et al., 2018). By comparison, face-wide melting occurs along the entire glacial face as a result of either convection (Magorrian & Wells, 2016) or fjord circulation (Bartholomaeus et al., 2013). Estimates of face-wide melt rates range widely, but are generally below 1 meter per day

(and may be up to $\mathcal{O}(10^6)$ m³/day of volumetric melt, based on an average glacial face area). Yet, only recently have studies considered the possibility that existing parameterizations of the ice-ocean boundary layer may be underestimating the contribution of face-wide melt (Jackson et al., 2019; Slater et al., 2018).

Fjord circulation has primarily been studied in the context of an estuary-like overturning circulation where warm and salty open-ocean water masses flow into the fjords at depth, and colder and fresher water masses flow out of the fjord at shallower depths (Stigebrandt, 1981; Farmer & Freeland, 2021; Inall & Gillibrand, 2010; Cottier et al., 2010). However, compared to most estuaries (Geyer & MacCready, 2014), deep glacial fjords in Greenland have relatively weak tidal influence and most of the vertical mixing is posited to occur near the glacial face (Straneo & Cenedese, 2015). The focus of previous 2D and 3D simulations of the shelf-to-fjord system has been to understand the sensitivity of glacial melt and the overturning circulation/fjord renewal to various fjord characteristics and atmospheric/oceanic drivers (e.g., Gladish et al. (2015), Sciascia et al. (2013), Xu et al. (2012), and Jackson et al. (2018)).

So far there are very few process-oriented models or theoretical efforts to quantify the interaction between fjord circulation and glacial melt rate within fjords. Along with the relative scarcity of ocean observations near marine-terminating glaciers, only recently has the horizontal recirculation within fjords and their sensitivity to fjord and forcing parameters received attention in models (Zhao et al., 2019, 2021), which has been suggested to have an influence on the face-wide melt rates (Slater et al., 2018; Jackson et al., 2019; Zhao et al., 2021; Carroll et al., 2017). Existing melt parameterizations either do not take into account horizontal near-glacier velocities (e.g., Sciascia et al. (2013), Xu et al. (2012)) or do not resolve the horizontal flows necessary for accurate melt rate predictions (e.g., Cowton et al. (2015), Carroll et al. (2017)). To remedy this, bulk glacial melt parameterizations should ideally use either near-glacier horizontal velocities based on resolved circulations or use predictions of near-glacier horizontal velocities in terms of the fjord forcing, geometry, and stratification.

To better understand these processes, we conduct a process-oriented exploration of fjord parameter space using simulations that can finely resolve the near-glacier horizontal circulation. We support these simulations with simple dynamical theories of overturning circulation, horizontal recirculation in the fjord interior, and glacial melt rate. Using these results, we address a gap in understanding of how fjord circulation and glacial melt co-interact, which has important implications for glacial retreat at the oceanic margins of ice sheets.

2 Fjord Model Setup

2.1 Model Configuration

To examine the interaction of fjord circulation and glacial melt, we use the Massachusetts Institute of Technology general circulation model (MITgcm, Marshall et al. (1997)) in a series of idealized high-resolution simulations. Our model uses an idealized geometric representation of a simple bathtub-like fjord-only domain with sloping side walls, a glacier face along its western boundary, and a Gaussian zonal sill centered at $x_S = 20$ km (see Fig. 1a). The model domain dimensions are $L \times W \times H = 25 \text{ km} \times 6 \text{ km} \times 800 \text{ m}$. There is quadratic bottom drag with a coefficient of 2×10^{-3} and no surface forcing. The eastern boundary region is nudged to a prescribed open ocean stratification in our reference experiment, based on near-fjord mouth observations from Ilulissat Icefjord (Gladish et al., 2015; Straneo & Cenedese, 2015), and includes a barotropic tidal velocity boundary condition in two of our perturbation experiments. See supplemental materials S-1 for further information on the model setup.

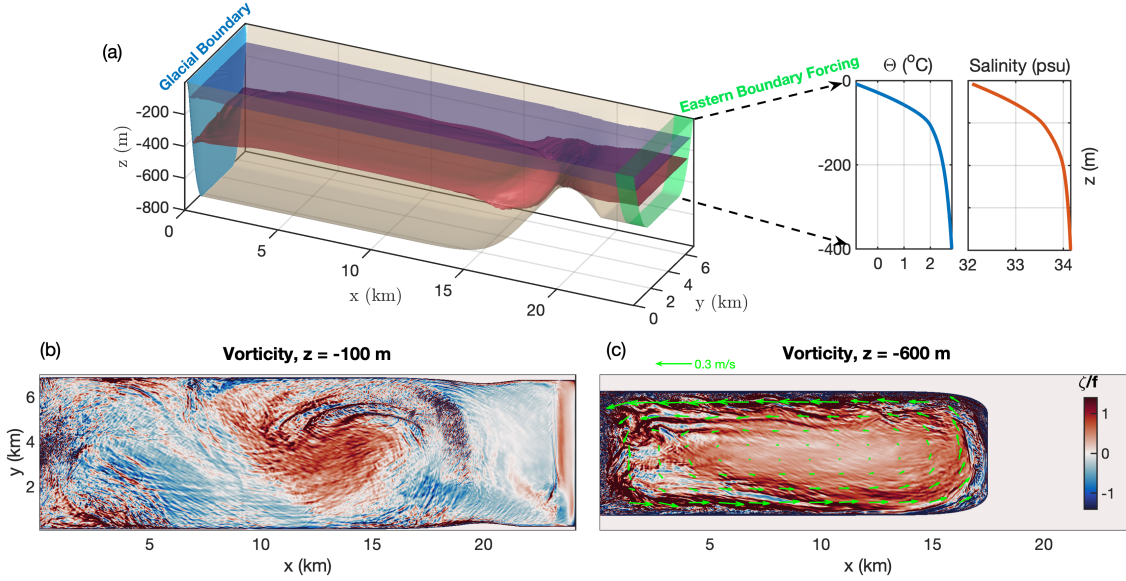


Figure 1. Reference simulation as specified in Section 2.2 showing (a) fjord geometry with two density interfaces $\sigma = 27.2$ (dark blue), 27.6 (red) kg/m³ and the eastern boundary temperature and salinity forcing; and (b),(c) contemporaneous snapshots of normalized vorticity at $z = -100$ m and $z = -600$ m, respectively. Velocity quivers are included in panel (c).

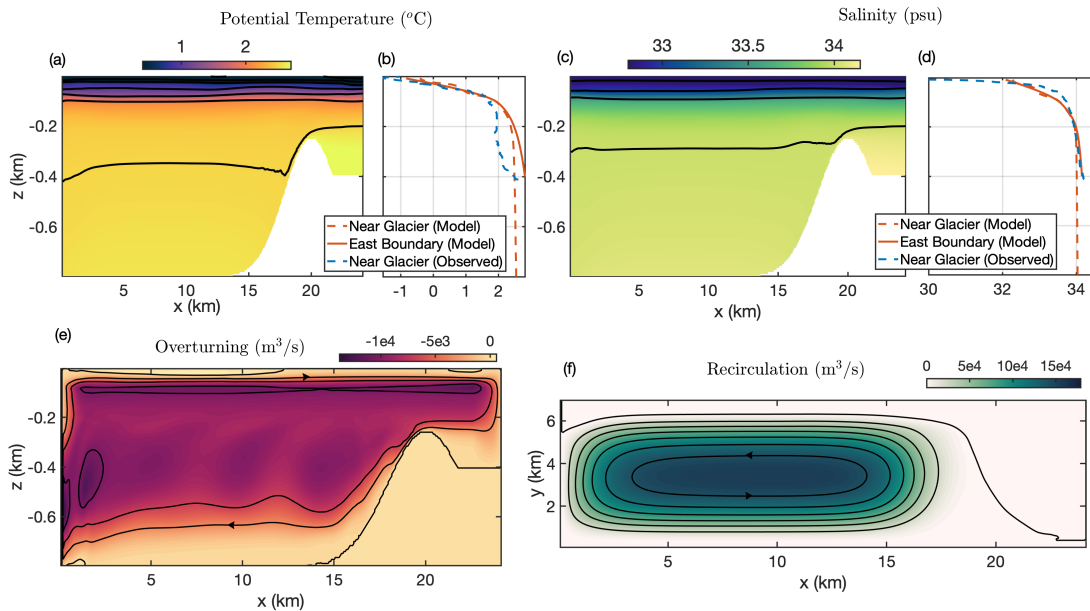


Figure 2. Time-averaged profiles of (a) meridionally-averaged temperature, (c) meridionally-averaged salinity with (b, d) model/observation comparisons using Ilulissat Icefjord data (Gladish et al., 2015; Straneo & Cenedese, 2015), and (e) meridionally-integrated overturning streamfunction, and (f) vertically-integrated recirculation strength over the bottom 600 m. The contour spacings are 0.5 °C, 0.5 psu, 3×10^3 m³/s, and 2×10^4 m³/s, in panels (a)-(d) respectively.

On the western boundary, the model is forced by a subglacial discharge plume parameterization at the fjord midpoint ($x = 0$, $y = W/2$) and a face-wide melt plume parameterization across the glacial face. Both plume parameterizations are based on buoyant plume theory, as described in Cowton et al. (2015). The plume parameterization solves 1D equations for mass and momentum conservation vertically along the plume, while heat and salt evolve in response to advection, entrainment of ambient waters, and the turbulent transfer to the ice face (Hellmer & Olbers, 1989). The plume is coupled to the circulation and stratification, allowing us to study feedbacks between plume dynamics and the fjord circulation. See supplemental materials S-1 for further discussion of both plume parameterizations.

The model horizontal resolution is 38 m and the vertical resolution is 8 m. We use a Smagorinsky biharmonic horizontal viscosity and the K-Profile Parameterization (KPP) of the vertical viscosity and diffusivity (Smagorinsky, 1963; Large et al., 1994), in addition to a background vertical diffusivity of $10^{-6} \text{ m}^2 \text{ s}^{-1}$. We use an f -plane approximation with a representative Coriolis parameter of $f = 1.31 \times 10^{-4} \text{ s}^{-1}$, corresponding to latitudes in central Greenland. The model experiments are run for 1 year because the fjord recirculation adjusts slowly and requires multiple months of spinup for some of the test cases, and all results shown (unless otherwise specified) are time-averaged over the last month.

2.2 A Reference Case

Fig. 1 illustrates the setup and circulation of our reference simulation. We impose a subglacial discharge plume of $Q_0 = 100 \text{ m}^3/\text{s}$, as well as a face-wide melt plume. For reference, most subglacial discharge plumes around Greenland range from 0 to $1000 \text{ m}^3/\text{s}$ with most fjords at the weaker end of this range (Mankoff et al., 2020). The reference case fjord dimensions are specified in Section 2.1 with a sill maximum at $z = -250 \text{ m}$ depth and a stratification similar to Ilulissat fjord (e.g., Gladish et al., 2015; Straneo & Cenedese, 2015) with no tidal forcing. The reference case parameters are shown in supplemental materials Table S1.

The vorticity snapshots at $z = -100 \text{ m}$ and $z = -600 \text{ m}$ in Fig. 1b, c suggest intense submesoscale variability based on the vorticity magnitude and structures generated near the sill overflow, boundary current, and plume outflow. At depth, the sill-crossing overflow (located at $x = 18.5 \text{ km}$) drives energetic small-scale variability and vorticity. The overflow also feeds a cyclonic boundary current, which periodically becomes unstable and sheds eddies into the interior (see supplemental materials Fig. S1). At shallower depths, the plume outflow is the dominant source of variability and is greatest at the neutral buoyancy depth (near $z = -100 \text{ m}$). The intrafjord submesoscale variability likely plays an important role in fjord stratification and mixing, circulation, and melt rates, but a more complete exploration will be deferred to a future study.

To illustrate the simulated fjord state, in Fig. 2 we plot profiles of time- and meridionally-averaged potential temperature and salinity, and compare them with observations from Illulisat Icefjord (Gladish et al., 2015; Straneo & Cenedese, 2015). The profiles of potential temperature and salinity at the ice face vs. the mouth of the fjord (panels (b) and (d)) show the effect of the water mass transformation driven by the near-glacier plumes. The modification of the inflowing water properties is more pronounced in the observations (Beaird et al., 2017) because we use a smaller discharge in our reference simulations than is observed in Illulisat Icefjord.

We quantify the fjord overturning circulation via the overturning streamfunction (Fig. 2e), which is calculated via

$$\psi(x, z) = \int_0^W \int_{z_B(x,y)}^z \bar{u} \, dz' \, dy'. \quad (1)$$

Here, \bar{u} is the time-averaged velocity in the x -direction (and defined to be 0 outside the bowl-shaped domain) and $z_B(x, y)$ is the bathymetric elevation. To quantify the horizontal recirculation, we first calculate the horizontal quasi-streamfunction

$$\Psi(x, y, z) = \int_0^y \bar{u} dy', \quad (2)$$

which is an approximation to the 3D streamfunction and is further discussed in supplemental materials S-2. We quantify the strength of the horizontal recirculation via the maximum value of the horizontal quasi-streamfunction in the region between the glacier face and the sill maximum:

$$R(z) = \max_{0 < x < 20 \text{ km}} \{\Psi(x, y, z)\}. \quad (3)$$

The vertically-integrated recirculation strength (over the bottom 600 m) is shown in Fig. 2f. The overturning and recirculation observed in our model results are idealized versions of the complex circulation observed in fjords with real geometries, but magnitudes are similar to those observed in nature (see Slater et al. (2018), Straneo and Cenedese (2015), and references therein).

3 Controls on Fjord Circulation and Glacial Melt

In order to understand the interaction of fjord circulation and glacial melt rate, we conduct a suite of experiments to test the effects of varying the glacial boundary layer parameterizations, discharge plume strength, geometric constraints, stratification, and tides. A complete list of the parameter ranges is shown in supplemental materials Table S1.

To understand the effect of the glacial face plumes on the fjord circulation and its feedback on melt rates, we compare four cases: the reference case and three different melt parameterizations, as listed in supplemental materials Table S1. The reference case ($Q_{100}M_P$) includes a subglacial discharge plume with $Q_0 = 100 \text{ m}^3/\text{s}$ and a melt plume representing the face-wide melt (which for comparison, contributes a freshwater flux of approximately $40 \text{ m}^3/\text{s}$). We additionally test three cases: (1) only the melt plume and no discharge (Q_0M_P), (2) a boundary layer melt parameterization and no discharge (Q_0M_{BL} , using the 3-equation thermodynamics with no melt plume, based on Hellmer and Olbers (1989)), and (3) a discharge plume only (Q_{100}).

Fig. 3 shows how the near-glacier meridionally-integrated overturning streamfunction (using ψ from Eq. (1) and zonally-averaging over the near-glacier region, $0 < x < 5 \text{ km}$), recirculation strength (R , using Eq. (2)), and meridionally-averaged melt rate (M) vary for each of these four cases. The overturning, recirculation, and melt rate are comparatively negligible for the boundary layer-only case Q_0M_{BL} because it does not include entrainment into the melt plume, which drives most of the overturning in the Q_0M_P case. The overturning circulation of the Q_0M_P case peaks at a depth of -500 m , while the Q_{100} case peaks at the discharge plume neutral buoyancy depth of -100 m . The two plumes are approximately additive, i.e., the melt plume-only and discharge plume-only experiments can be added together to approximately obtain the overturning circulation in the reference case, which utilizes both plumes.

Fig. 3 suggests that there is an approximate correlation between overturning, recirculation, and melt rate with depth, which we will discuss further in Section 4. Contrary to expectations that discharge plumes (when active) drive a majority of the melt (Straneo & Cenedese, 2015), the melt plume case shows a total melt rate that is approximately 70% of the reference case melt rate. However, the rate of undercutting (defined here as the average melt rate over the bottom 200 m) for the two cases are nearly equal because although the overturning is weaker for this case, it is located deeper in the water column, where the warmer water recirculation drives a significant percentage of the

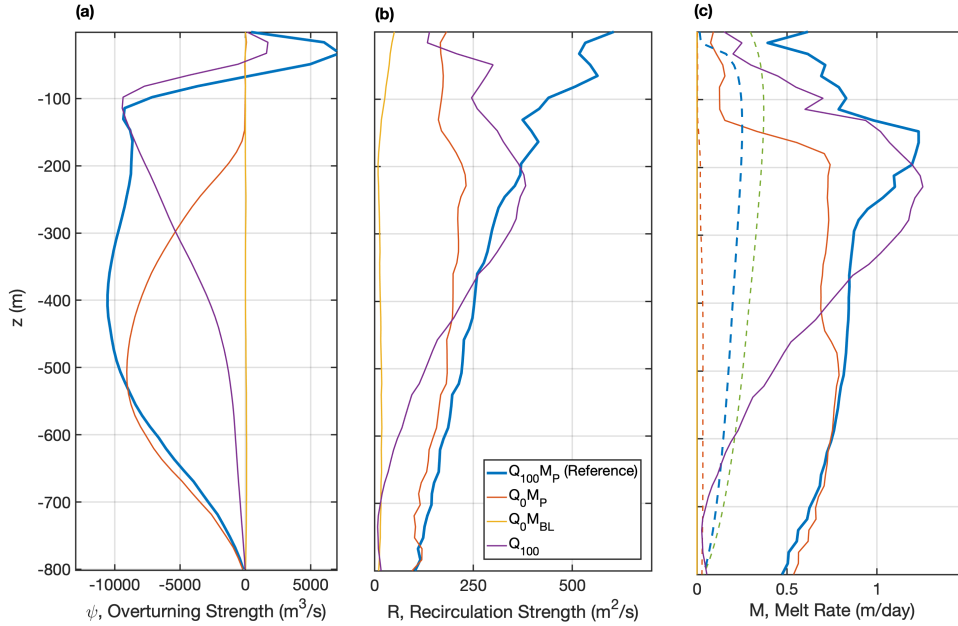


Figure 3. Profiles of (a) meridionally-integrated overturning streamfunction, (b) recirculation strength (as defined in Section 2.2), and (c) meridionally-averaged melt rate for the reference case ($Q_{100}M_P$), a melt plume only case (Q_0M_P), a boundary layer melt parameterization case (Q_0M_{BL}), and subglacial discharge only case (Q_{100}). The dotted lines in the melt rate panel show the direct contribution of the subglacial discharge plume to the meridionally-averaged melt rate.

209 melt rate. By comparison, the discharge plume-only case only accounts for 40% of the
 210 reference case melt rate because the overturning is located at shallower depths. Note also
 211 that most of the discharge plume-driven melt occurs over the face-wide area instead of
 212 the area where the plume is in contact with the glacial face (see Fig. 3c).

213 The sensitivity of the overturning, recirculation, and melt rates to discharge strength,
 214 sill height, fjord depth and width, stratification, and tides are also important and sim-
 215 ilarly show a correlation between vertical profiles of overturning, recirculation, and melt
 216 rate (see supplemental materials Figs. S2-S6 parameter sensitivity cross-section plots of
 217 temperature, salinity, overturning, recirculation, and melt rates). An important take-
 218 away is that increasing the discharge strength leads to diminishing increases in circula-
 219 tion strength and melt, i.e., increasing discharge has a strong effect for weaker discharge
 220 rates, but a significantly weaker effect on melt rates beyond the discharge rate of $Q =$
 221 $100 \text{ m}^3/\text{s}$ in the reference case. Increasing the discharge by an extreme factor of 10 (the
 222 $Q_{1000}M_P$ case) relative to the reference case increases the overturning by a factor a 2.5,
 223 but this only increases the melt rate by 30%. The reason for the diminished importance
 224 of discharge-driven melt is that increases in discharge primarily amplifies the shallow over-
 225 turning and recirculation, which has a smaller impact on the overall melt rate due to the
 226 colder waters present at these depths.

4 Linking Fjord Renewal, Horizontal Circulation, and Melt

In order to understand the sensitivity of glacial melt rates to fjord parameters, we extend previous theories (Zhao et al., 2021) to relate the fjord overturning, recirculation, and melt to the parameters studied in Section 3.

4.1 Overturning Theory

Our theory for the overturning circulation uses the sum of the discharge plume entrainment and the melt plume entrainment (Morton et al., 1956; Cowton et al., 2015; Straneo & Cenedese, 2015):

$$\psi(x = 0, z) \approx \beta_p B^{1/3} (z - z_B)^{5/3} + \beta_m W \left(\frac{\rho_w g'_0}{\rho_i} \right)^{1/3} M_0^{1/3} (z - z_B)^{4/3}. \quad (4)$$

Here, $\beta_p = (6/5)(9/5)^{1/3}\pi^{1/3}\epsilon^{4/3}$ (entrainment factor for a half-cone plume) and $\beta_m = (3/4)(4/5)^{1/3}\epsilon^{2/3}$ (entrainment factor for a sheet plume), which depend on an experimentally-derived entrainment coefficient, $\epsilon = 0.13$ (Linden, 2000). Additionally, M_0 is the melt rate (assumed to be constant with depth in the uniform density region) and ρ_w and ρ_i are the density of fresh water and ice, respectively. The discharge plume buoyancy flux $B(z) = g'Q$ varies with depth, but assuming an approximately uniform background density (ρ) below the neutral buoyancy depth yields $B \approx B_0 = g'_0 Q_0$, where B_0 is the buoyancy flux at the plume source, Q_0 is the subglacial discharge rate, and the reduced gravity is $g'_0 = g(\rho - \rho_w)/\bar{\rho}$. The neutral buoyancy depth of the discharge plume is primarily dependent on background stratification and weakly sensitive to the water mass transformation rates.

The melt plume buoyancy flux (last term in Eq. (4)) uses a simplified depth-constant melt rate M_0 , but this can be extended to a depth-varying melt rate $M(z)$ and both the discharge plume and melt plume buoyancy flux contributions may be extended to depth-varying background density and solved numerically (see supplemental materials S-1 for further details). Our simulations suggest that the depth variation of $M(z)$ is proportional to the time-mean near-glacier along-face velocity $\bar{v}(z)$ via the relationship $M(z) \approx k_M \bar{v}(z)$ for a proportionality constant $k_M \approx 0.035$, which is further discussed in Section 4.3. This relationship suggests a potential feedback between melt, overturning, and horizontal recirculation.

4.2 Recirculation Theory

In order to understand the relationship between overturning and recirculation, we apply the scaling arguments from Zhao et al. (2021) based on the vorticity balance. This shows that below the neutral buoyancy depth (which can be predicted using plume theory; see supplemental materials S-1), vorticity generated by water mass transformation due to the glacial boundary conditions (both the melt plume and discharge plume) is primarily balanced by the curl of bottom drag (as evidenced by supplemental materials Fig. S7).

Based on an approximate balance between these two vorticity terms, we derive the following scaling relationship between the overturning streamfunction and recirculation

$$\langle \psi(x, z) \rangle_x \approx \frac{C_F C_d}{f L_r^2 H_b^2} \left(\int_{-H}^z R(z') dz' \right)^2. \quad (5)$$

Here, $C_F = 2(W + x_S)$ is the circumference of the fjord recirculation region, $C_d = 2 \times 10^{-3}$ is the bottom drag coefficient, and the boundary current width L_r is empirically approximated by $L_r \sim (L_d + W/2)/2$ for a deformation radius L_d . We use the zonal average of the overturning streamfunction $\langle \psi(x, z) \rangle_x$ over the near-plume region $0 < x < L_r$ as a numerical approximation to the plume-driven overturning $\psi(x = 0, z)$ from Eq.

272 (4). The water column thickness of the recirculation region below the neutral depth is
 273 $H_b = H - |z_N|$, where z_N is the neutral depth and H is the depth of the fjord. See
 274 Zhao et al. (2021) for a more detailed discussion of this scaling theory.

275 4.3 Melt Rate Theory

276 In order to extend our predictions of recirculation to total melt rate, we apply an-
 277 other scaling approximation from Zhao et al. (2021) that relates the time-mean horizon-
 278 tal tangential velocity $\bar{v}(z)$ at the glacial face to the horizontal recirculation, expressed
 279 as $\bar{v}(z) \approx 2R(z)/(L_r H_b)$. Assuming that the melt rates are primarily driven by hori-
 280 zontal velocities, which is true for the majority of the glacial surface area, the 3-equation
 281 thermodynamics (using e.g., Hellmer and Olbers (1989), D. M. Holland and Jenkins (1999)
 282 and assuming ice temperatures that are close to boundary layer ocean temperatures) al-
 283 lows us to simplify this relationship to a linear melt rate $M(z)$ (in m/s) that is approx-
 284 imately proportional to $\bar{v}(z)$ (and thus, $R(z)$),

$$285 \quad M(z) = \frac{c_w(T_p - T_b)}{L_i + c_i(T_b - T_i)} C_d^{1/2} \Gamma_T \sqrt{v^2 + w^2} \approx \underbrace{\frac{c_w(T_p - T_b)}{L_i} C_d^{1/2} \Gamma_T}_{\equiv k_M} |\bar{v}| \quad (6)$$

286 where $L_i = 3.35 \times 10^5 \text{ J kg}^{-1}$ is the latent heat of fusion of ice, $c_i = 2 \times 10^3 \text{ J kg}^{-1}$
 287 K^{-1} is the specific heat capacity of ice, $c_w = 3.974 \times 10^3 \text{ J kg}^{-1} \text{ K}^{-1}$ is the specific
 288 heat capacity of water, $C_d = 2 \times 10^{-3}$ is the bottom drag coefficient, $\Gamma_T = 2.2 \times 10^{-2}$
 289 is the thermal transfer constant, and T_b , T_p , T_i are the boundary layer, plume, and ice
 290 temperature, respectively. For further discussion on this melt rate approximation, see
 291 supplemental materials S-4.

292 4.4 Summary of Theories

293 We can rewrite the relationships in Eqs. (4)-(6) and the plume theory (in supple-
 294 mental materials S-1) as a priori predictions for the bulk overturning, recirculation, and
 295 melt rate explicitly in terms of the subglacial discharge, fjord width and depth, strat-
 296 ification, and near-glacier horizontal velocity.

297 The bulk overturning strength prediction (i.e., the overturning streamfunction in
 298 Eq. (4) evaluated at the neutral buoyancy depth z_N) can be expressed as

$$299 \quad \psi(z_N) \approx \beta_p (g'_0 Q_0)^{1/3} (z_N - z_B)^{5/3} + \beta_m W \left(\frac{\rho_w g'_0}{\rho_i} \right)^{1/3} (k_M \langle \bar{v} \rangle_z)^{1/3} (z_N - z_B)^{4/3}. \quad (7)$$

300 Fig. 4a and 4b show the predicted vs. simulation-diagnosed values of the neutral buoy-
 301 ancy depth based on plume theory and the overturning strength, respectively. These two
 302 comparisons show that over the range of parameters, the neutral buoyancy depth is well-
 303 approximated by plume theory (see e.g., Turner (1979)), with a squared correlation co-
 304 efficient of 0.92; similarly, overturning strength is well-approximated by Eq. (7), with a
 305 squared correlation coefficient of 0.89.

306 Using Eq. (5) and (7), we can express the depth-averaged recirculation below the
 307 neutral buoyancy depth in terms of the bulk overturning strength

$$308 \quad \langle R \rangle_z \approx \left(\frac{\psi(z_N) f L_r^2}{C_F C_d} \right)^{1/2}, \quad (8)$$

309 or less accurately (as was used in the melt rate theory in Eq. (6)), the depth-averaged
 310 along-face zonal velocity

$$311 \quad \langle R \rangle_z \approx L_r (H + z_N) \langle \bar{v} \rangle_z / 2. \quad (9)$$

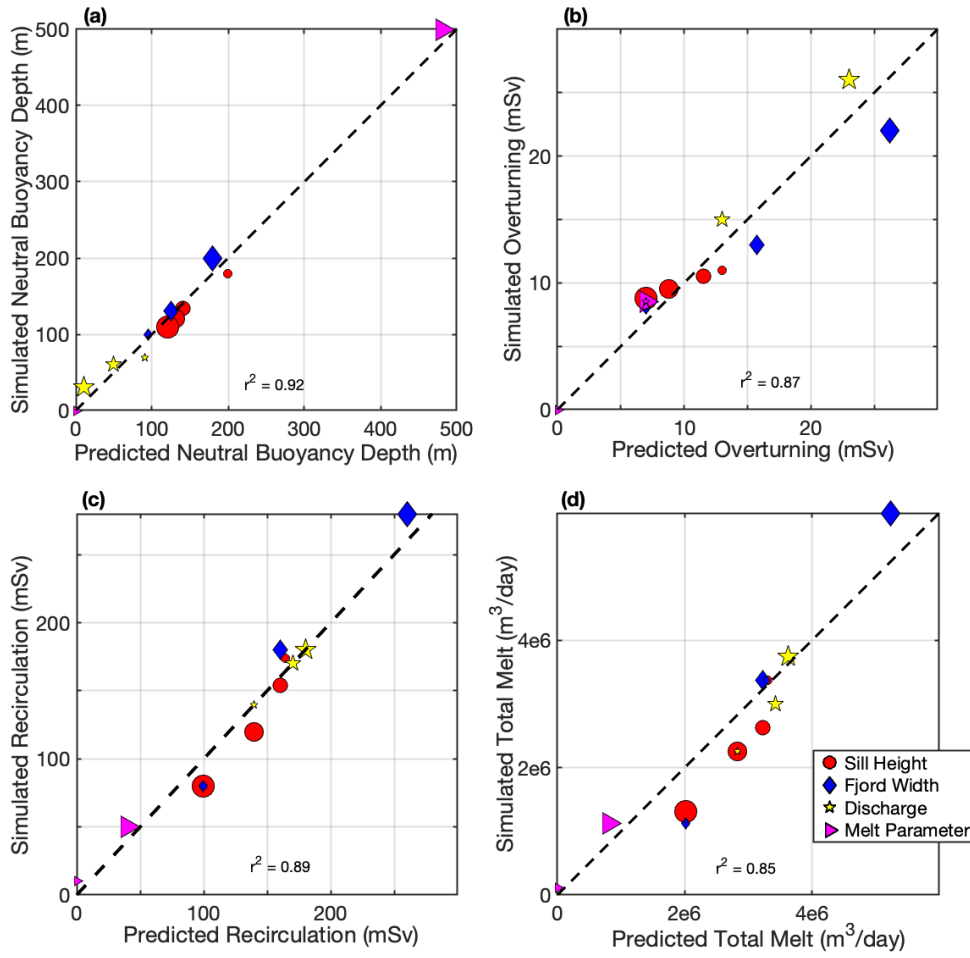


Figure 4. Simulation-diagnosed vs. theoretical predictions for (a) the neutral buoyancy depth based on plume theory, (b) the overturning circulation based on plume theory (Eq. (7)), (c) the depth-averaged recirculation based on the bulk overturning strength (Eq. (8)), and (d) the overall glacial melt rate based on the recirculation theory (Eq. (11)).

312 We note that equating the approximations in Eq. (8) and (9) allows us to relate the bulk
 313 overturning to the depth-averaged near-glacier along-face velocity,

$$314 \quad \langle \bar{v} \rangle_z \approx \frac{2f\psi(z_N)}{C_F C_d (H + z_N)}, \quad (10)$$

315 thereby removing the dependence of these theories on $\langle \bar{v} \rangle_z$, which is an essential (albeit
 316 less accurate) step to making the melt theory fully predictive i.e., without requiring a
 317 priori knowledge of the along-glacier velocity.

318 Fig. 4c shows a comparison between the predicted depth-averaged recirculation be-
 319 low the neutral buoyancy depth using Eq. (8) and the corresponding simulation-diagnosed
 320 recirculation using Eq. (2). The recirculation above the neutral buoyancy depth is not
 321 included since vorticity advection primarily balances water mass transformation above
 322 this depth and the assumptions used for the scaling arguments used to derive Eqs. (5)
 323 and (8) no longer apply. Additionally, the melt rates in this region only account for a
 324 small percentage of the overall melt rate since the outflowing glacially-modified water
 325 masses are much colder. However, the recirculation at depths between the sill maximum
 326 and the neutral buoyancy depth are taken into account in Eqs. (5) and (8). Fig. 4c shows
 327 that over the range of parameters, recirculation varies over a large range, but is well-
 328 approximated by this simple scaling argument, with a squared correlation coefficient of
 329 0.89.

330 Finally, the depth-averaged melt rate can be expressed as

$$331 \quad \langle M \rangle_z \approx k_M \langle \bar{v} \rangle_z. \quad (11)$$

332 Fig. 4d shows a comparison between the predicted depth-averaged melt rate calculated
 333 from Eq. (11) multiplied by the glacial surface area and the corresponding value diag-
 334 nosed from the simulation by integrating the melt rate over the entire glacial face. This
 335 shows that over the range of parameters, melt rate varies significantly, but is relatively
 336 well-approximately by this simple scaling argument. Although the prediction of total melt
 337 rate is less accurate (with a squared correlation coefficient of 0.85) than the predicted
 338 recirculation, this is likely because the melt rate theory requires additional approxima-
 339 tions and assumptions. The melt rate can also be (less accurately) related to the bulk
 340 overturning strength or depth-averaged recirculation using Eqs. (10) and (9), respectively,
 341 to remove the dependence on the the near-glacier along-face velocity. The fully predic-
 342 tive theory for the total melt rate in terms of the overturning streamfunction by substi-
 343 tuting Eq. (10) in Eq. (11) is compared with the simulation diagnosed melt rate in Fig.
 344 S8 (which has a squared correlation coefficient of 0.72).

345 5 Discussion and Conclusion

346 In this study, we use a high-resolution idealized model (see Section 2) to analyze
 347 the sensitivity of glacial melt to fjord circulation (in Section 3) and address an impor-
 348 tant gap in scientific understanding: how fjord circulation and glacial melt co-influence
 349 each other and how to predict their bulk values as a function of fjord parameters. To achieve
 350 this, we extended previous theories (in Section 4) to predict the overturning, recircula-
 351 tion, and melt rates as functions of the model fjord parameters. These relationships are
 352 summarized in Eqs. (7)-(11), which explicitly express the sensitivity of the circulation
 353 and melt to each of the fjord parameters and illustrate the melt-circulation feedback, us-
 354 ing the near-glacier velocity as a common link.

355 We found that a majority of the glacial melt occurs over the entire glacial front,
 356 instead of being localized to the discharge plume. For the highest discharge case ($Q_{1000} \text{MP}$),
 357 the discharge plume region accounts for only 26% of the overall melt (and only 18% for
 358 the reference case) even though it increases the peak overturning strength by a factor

359 of 2.5, because it confines this overturning to a narrow depth range near the neutral buoy-
360 ancy depth. Most of the parameter variations we studied had a significant impact on the
361 overall melt rate (see supplemental materials Fig. S6 for a figure showing the sensitiv-
362 ity of glacial melt distributions to fjord properties). These variations in melt can be the-
363 oretically related to the recirculation and overturning circulation, which in turn have two
364 drivers: a face-wide melt plume and a discharge plume.

365 The discharge plume drives a shallower overturning than the face-wide melt plume
366 and, therefore, the face-wide melt plays a significantly larger role in glacial melt because
367 it provides a greater proportion of the deep overturning. In this deep overturning cir-
368 culation, warm water masses flow toward the glacial face at a range of depths primar-
369 ily in the deeper half of the fjord, and flows away in the upper half (see the Q_0M_P case
370 in Fig. 2a). Our results show that over most of the fjord parameter range studied, the
371 deep overturning within fjords is primarily driven by melt, and the overall melt is pri-
372 marily driven by recirculation at depth, which is correlated with the deep overturning
373 circulation. This glacial melt seems to be concentrated at depth due to the warm wa-
374 ter available at these depths, where the stratification is weaker. Additionally, the warm-
375 water renewal in the deeper waters of the fjord is more strongly controlled by face-wide
376 melt compared to the subglacial discharge plume. This potentially has implications that
377 fjords with weak subglacial discharge year-round or in wintertime conditions can still have
378 substantial melt rates as long as warm water is present within the fjord. There is obser-
379 vational evidence that suggests this may occur in some fjords (Wood et al., 2018), but
380 more wintertime glacial melt rate observations are needed to confirm this phenomenon.

381 There are numerous caveats in this study due to the limitations of our simple model
382 configuration. These include the simplicity of fjord geometry, atmospheric forcing, ver-
383 tical mixing representation, the lack of sea ice, mélange, and icebergs, which can sup-
384 ply substantial buoyancy input (Beaird et al., 2017). As a result of the high-resolution
385 fjord-only domain, a caveat is the prescription of the eastern open-ocean boundary. The
386 eastern boundary in our model is nudged to the open-ocean stratification, which is fixed
387 for our simulation, so the boundary likely does not capture all of the variability that a
388 fjord-shelf system would be able to include; there can be a shelf current-induced increase/
389 decrease in the exchange between the fjord and shelf (Zhao et al., 2021). We also do not
390 consider the effect of winds, which likely exhibits a larger effect on the shelf region via
391 fjord overturning driven by coastal upwelling (not included in our domain), but may also
392 directly drive fjord circulation/renewal for strong enough katabatic wind events (Zhao
393 et al., 2021; Spall et al., 2017). Although this choice is an imperfect one, the eastern bound-
394 ary is nudged to fjord mouth observations (from Gladish et al. (2015)); in reality, a do-
395 main that includes the shelf would likely establish a balance between the shelf stratifi-
396 cation and near-glacial stratification to set the stratification at the fjord mouth (e.g., Zhao
397 et al. (2021)). Also, in our glacial boundary parameterization, the melt rates are calcu-
398 lated using the closest grid point of horizontal and vertical fjord velocities, which is an
399 imperfect representation; in general, a better understanding and representation of the
400 ice-ocean boundary layer needed to improve glacial melt rate estimates.

401 Following this study, there are a number of open questions that require further at-
402 tention. Additional work is needed to investigate the submesoscale phenomenology and
403 the distribution of mixing within the fjord. Another future avenue is to investigate bound-
404 ary layer parameterizations at the glacial face and the interaction of submesoscale-microscale
405 dynamics. A final avenue is to investigate the interaction between circulation and melt
406 in more realistic regional models and the co-interaction of multiple neighboring fjords.

407 **Acknowledgments**

408 This material is based in part upon work supported by the NASA FINESST Fel-
409 lowship under Grant 80NSSC20K1636 and the National Science Foundation under Grant

OCE-1751386. This work used the Extreme Science and Engineering Discovery Environment (XSEDE, Towns et al. (2014)), which is supported by National Science Foundation grant number ACI-1548562. The MITgcm model configuration, test case, and modified plume parameterization (a slightly modified version of Cowton et al. (2015)) is available at: <https://doi.org/10.5281/zenodo.5214142>.

References

- Bartholomaeus, T. C., Larsen, C. F., & O’Neel, S. (2013). Does calving matter? Evidence for significant submarine melt. *Earth Planet. Sci. Lett.*, *380*, 21–30. doi: 10.1016/j.epsl.2013.08.014
- Beaird, N., Straneo, F., & Jenkins, W. (2017). Characteristics of Meltwater Export from Jakobshavn Isbrae and Ilulissat Icefjord. *Ann. Glaciol.*, *58*(74), 107–117. doi: 10.1017/aog.2017.19
- Carroll, D., Sutherland, D. A., Shroyer, E., Nash, J. D., Catania, G., & Stearns, L. A. (2017). Subglacial discharge-driven renewal of tidewater glacier fjords. *J. Geophys. Res. Oceans*, *122*, 6611–6629.
- Chauché, N., Hubbard, A., Gascard, J. C., Box, J. E., Bates, R., & Koppes, e. a., M. (2014). Ice-ocean interaction and calving front morphology at two west greenland tidewater outlet glaciers. *Cyrosphere*, *8*, 1457–1468. doi: doi.org/10.5194/tc-8-1457-2014
- Cottier, F., Nilsen, F., Skogseth, R., Tverberg, V., Skardhamar, J., & Svendsen, H. (2010, 11). Arctic fjords: A review of the oceanographic environment and dominant physical processes. *Geological Society of London Special Publications*, *344*, 35–50. doi: 10.1144/SP344.4
- Cowton, T., Slater, D., Sole, A., Goldberg, D., & Nienow, P. (2015). Modeling the impact of glacial runoff on fjord circulation and submarine melt rate using a new subgrid-scale parameterization for glacial plumes. *J. Geophys. Res. Oceans*, *120*, 796–812.
- Cowton, T., Sole, A. J., Nienow, P. W., Slater, D. A., & Christoffersen, P. (2018). Linear response of east greenland’s tidewater glaciers to ocean/atmosphere warming. *Proc. Natl. Acad. Sci. (USA)*, *115*(31), 7907–7912. doi: 10.1073/pnas.1801769115
- Farmer, D., & Freeland, H. (2021). The physical oceanography of fjords. *Prog. Oceanogr.*, *12*, 147–220.
- Fried, M. J., Catania, G. A., Stearns, L. A., Sutherland, D. A., Bartholomaeus, T. C., Shroyer, E., & Nash, J. (2018). Reconciling drivers of seasonal terminus advance and retreat at 13 central west greenland tidewater glaciers. *J. Geophys. Res. Earth Surface*, *123*(7), 1590–1607. doi: doi.org/10.1029/2018JF004628
- Geyer, W. R., & MacCready, P. (2014). The Estuarine Circulation. *Annu. Rev. Fluid Mech.*, *46*(1), 175–197. doi: 10.1146/annurev-fluid-010313-141302
- Gladish, C. V., Holland, D. M., Rosing-Asvid, A., Behrens, J. W., & Boje, J. (2015). Oceanic Boundary Conditions for Jakobshavn Glacier. Part I: Variability and Renewal of Ilulissat Icefjord Waters, 200114. *J. Phys. Oceanogr.*, *45*(1), 3–32. doi: 10.1175/JPO-D-14-0044.1
- Hellmer, H. H., & Olbers, D. J. (1989). A two-dimensional model for the thermohaline circulation under an ice shelf. *Antarctic Science*, *1*(4), 325–336. doi: 10.1017/S0954102089000490
- Holland, D. M., & Jenkins, A. (1999). Modeling Thermodynamic Ice-Ocean Interactions at the Base of an Ice Shelf. *J. Phys. Oceanogr.*, *29*(8), 1787–1800. doi: 10.1175/1520-0485(1999)029<1787:MTIOIA>2.0.CO;2
- Holland, P. R., Jenkins, A., & Holland, D. M. (2008). The response of ice shelf basal melting to variations in ocean temperature. *J. Climate*, *21*, 2258–2272. doi: 10.1175/2007JCLI1909.1

- 462 Inall, M. E., & Gillibrand, A., P. (2010). The physics of mid-latitude fjords: a re-
463 view. *Geological Society of London Special Publications*, *344*, 17–33.
- 464 Jackson, R. H., Lentz, S. J., & Straneo, F. (2018). The Dynamics of Shelf Forcing in
465 Greenlandic Fjords. *J. Phys. Oceanogr.*, *48*(11), 2799–2827. doi: 10.1175/JPO
466 -D-18-0057.1
- 467 Jackson, R. H., Nash, J. D., Kienholz, C., Sutherland, D. A., Amundson, J. M.,
468 Motyka, R. J., ... Pettit, E. (2019). Meltwater intrusions reveal mechanisms
469 for rapid submarine melt at a tidewater glacier. *Geophys. Res. Lett.*. doi:
470 10.1029/2019GL085335
- 471 Linden, P. F. (2000). *Convection in the environment. In Perspectives in Fluid Dy-*
472 *namics, ed. GK Batchelor, HK Moffat, MG Worster.* Cambridge, U.K.: Cam-
473 bridge University Press.
- 474 Magorrian, S. J., & Wells, A. J. (2016). Turbulent plumes from a glacier terminus
475 melting in a stratified ocean. *J. Geophys. Res. Oceans*, *121*(7), 4670–4696. doi:
476 10.1002/2015JC011160
- 477 Mankoff, K. D., Noël, B., Fettweis, X., Ahlstrm, A. P., Colgan, W., Kondo, K.,
478 ... Fausto, R. S. (2020). Greenland liquid water discharge from 1958
479 through 2019. *Earth Syst. Sci. Data*, *12*, 2811–2841. doi: doi.org/10.5194/
480 essd-12-2811-2020
- 481 Marshall, J. A., Hill, C., Perelman, L., & Heisey, C. (1997). A finite-volume, incom-
482 pressible navier stokes model for studies of the ocean on parallel computers. *J.*
483 *Geophys. Res.*, *102* (C3), 5753–5766.
- 484 Morlighem, M., Bondzio, J., Seroussi, H., Rignot, E., Larour, E., Humbert, A., &
485 Rebuffi, S. (2016). Modeling of store gletschers calving dynamics, west green-
486 land, in response to ocean thermal forcing. *Geophys. Res. Lett.*, *43*, 2659–2666.
487 doi: doi.org/10.1002/2016GL067695
- 488 Morton, B. R., Taylor, G. I., & Turner, J. S. (1956). Turbulent gravitational con-
489 vection from maintained and instantaneous sources. *Proceedings of the Royal*
490 *Society of London. Series A. Mathematical and Physical Sciences*, *234* (1196),
491 1–23. doi: 10.1098/rspa.1956.0011
- 492 Rignot, E., Fenty, I., Xu, Y., Cai, C., & Kemp, C. (2015). Undercutting of marine-
493 terminating glaciers in west greenland. *Geophys. Res. Lett.*, *42*(14), 5909–5917.
494 doi: doi.org/10.1002/2015GL064236
- 495 Sciascia, R., Straneo, F., Cenedese, C., & Heimbach, P. (2013). Seasonal variability
496 of submarine melt rate and circulation in an East Greenland fjord. *J. Geophys.*
497 *Res. Oceans*, *118*, 2492–2506.
- 498 Slater, D. A., Benn, D. I., Cowton, T. R., Bassis, J. N., & Todd, J. A. (2021).
499 Calving multiplier effect controlled by melt undercut geometry. *J. Geophys.*
500 *Res. Earth Surf.*, *n/a*(n/a), e2021JF006191. doi: https://doi.org/10.1029/
501 2021JF006191
- 502 Slater, D. A., Straneo, F., Das, S. B., Richards, C. G., Wagner, T. J. W., & Nienow,
503 P. W. (2018). Localized Plumes Drive Front-Wide Ocean Melting of A Green-
504 landic Tidewater Glacier. *Geophys. Res. Lett.*, *45*(22), 12,350 – 12,358. doi:
505 10.1029/2018GL080763
- 506 Spall, M. A., Jackson, R. H., & Straneo, F. (2017). Katabatic Wind-Driven Ex-
507 change in Fjords. *J. Geophys. Res. Oceans*, *122*(10), 8246–8262. doi: 10.1002/
508 2017JC013026
- 509 Stigebrandt, A. (1981). A mechanism governing the estuarine circulation in deep,
510 strongly stratified fjords. *Estuar. Coast. Mar. Sci.*, *13*, 197–211.
- 511 Straneo, F., & Cenedese, C. (2015). The Dynamics of Greenland’s Glacial Fjords
512 and Their Role in Climate. *Annu. Rev. Mar. Sci.*, *7*(1), 89–112. doi: 10.1146/
513 annurev-marine-010213-135133
- 514 Straneo, F., & Heimbach, P. (2013). North Atlantic Warming and the Retreat of
515 Greenland’s Outlet Glaciers. *Nature*, *504*(7478), 36–43. doi: https://doi.org/
516 10.1038/nature12854

- 517 Towns, J., Cockerill, T., Dahan, M., Foster, I., Gaither, K., Grimshaw, A., . . .
518 Wilkins-Diehr, N. (2014, Sept). XSEDE: Accelerating scientific discov-
519 ery. *Computing in Science & Engineering*, 16(5), 62-74. doi: 10.1109/
520 MCSE.2014.80
- 521 Turner, J. S. (1979). *Buoyancy effects in fluids*. Cambridge University Press Paper-
522 back.
- 523 van den Broeke, M. R., Enderlin, E. M., Howat, I. M., Munneke, P. K., Noël,
524 B. P. Y., van de Berg, W. J., . . . Wouters, B. (2016). On the recent con-
525 tribution of the Greenland ice sheet to sea level change. *The Cryosphere*, 10,
526 1933–1946. doi: 10.5194/tc-10-1933-2016
- 527 Wagner, T. J. W., James, T. D., Murray, T., & Vella, D. (2016). On the role of
528 buoyant flexure in glacier calving. *Geophys. Res. Lett.*, 43(1), 232–240A. doi:
529 doi.org/10.1002/2015GL067247
- 530 Wood, M., Rignot, E., Fenty, I., An, L., Bjørk, A., van den Broeke, M., . . . Zhang,
531 H. (2021). Ocean forcing drives glacier retreat in Greenland. *Science Advances*,
532 7(1). doi: 10.1126/sciadv.aba7282
- 533 Wood, M., Rignot, E., Fenty, I., Menemenlis, D., Millan, R., Morlighem, M.,
534 . . . Seroussi, H. (2018). Ocean-Induced Melt Triggers Glacier Retreat
535 in Northwest Greenland. *Geophys. Res. Lett.*, 45(16), 8334–8342. doi:
536 10.1029/2018GL078024
- 537 Xu, Y., Rignot, E., Menemenlis, D., & Koppes, M. (2012). Numerical experiments
538 on subaqueous melting of Greenland tidewater glaciers in response to ocean
539 warming and enhanced subglacial discharge. *Ann. Glaciol.*, 53 (60), 229–234.
- 540 Zhao, K. X., Stewart, A. L., & McWilliams, J. C. (2019). Sill-Influenced Exchange
541 Flows in Ice Shelf Cavities. *J. Phys. Oceanogr.*, 49 (1), 163–191. doi: 10.1175/
542 JPO-D-18-0076.1
- 543 Zhao, K. X., Stewart, A. L., & McWilliams, J. C. (2021). Geometric Constraints on
544 Glacial FjordShelf Exchange. *J. Phys. Oceanogr.*, 51 (4), 1223–1246. doi: 10
545 .1175/JPO-D-20-0091.1

Figure 1.

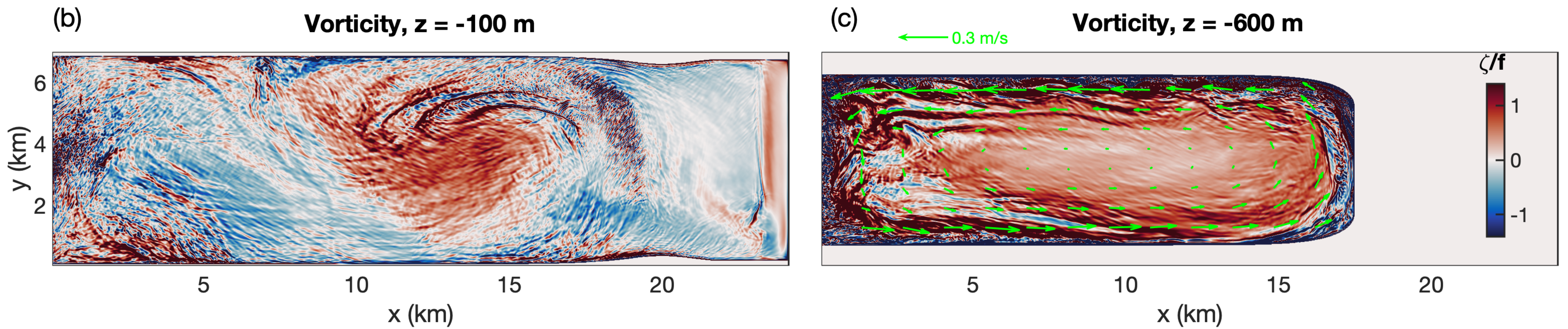
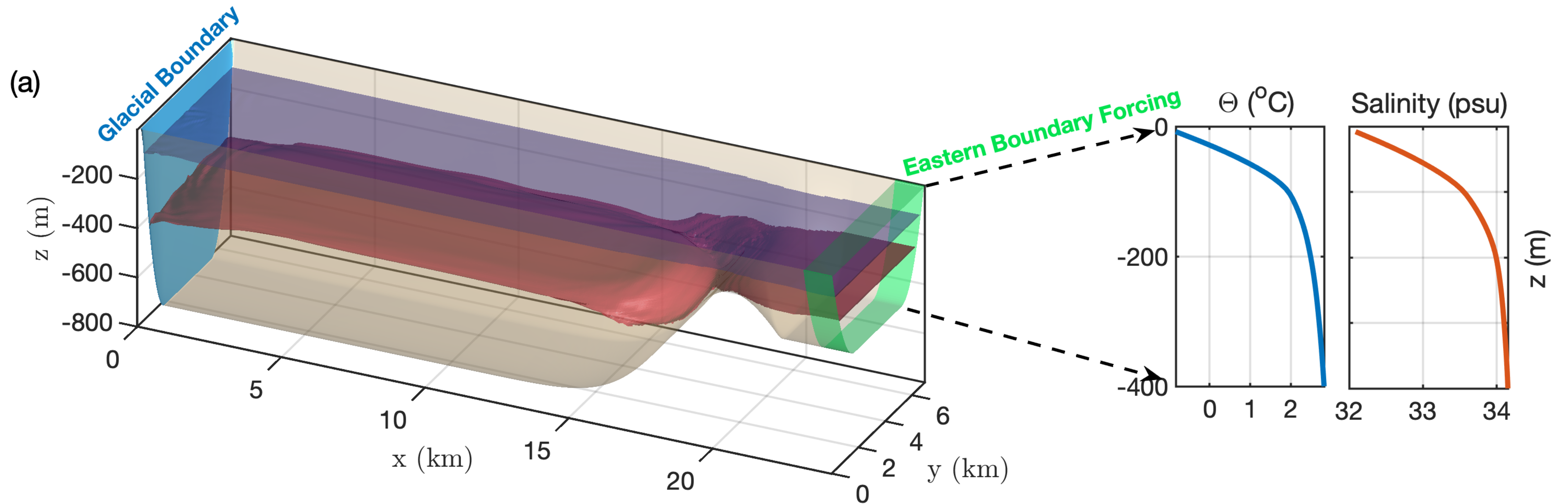


Figure 2.

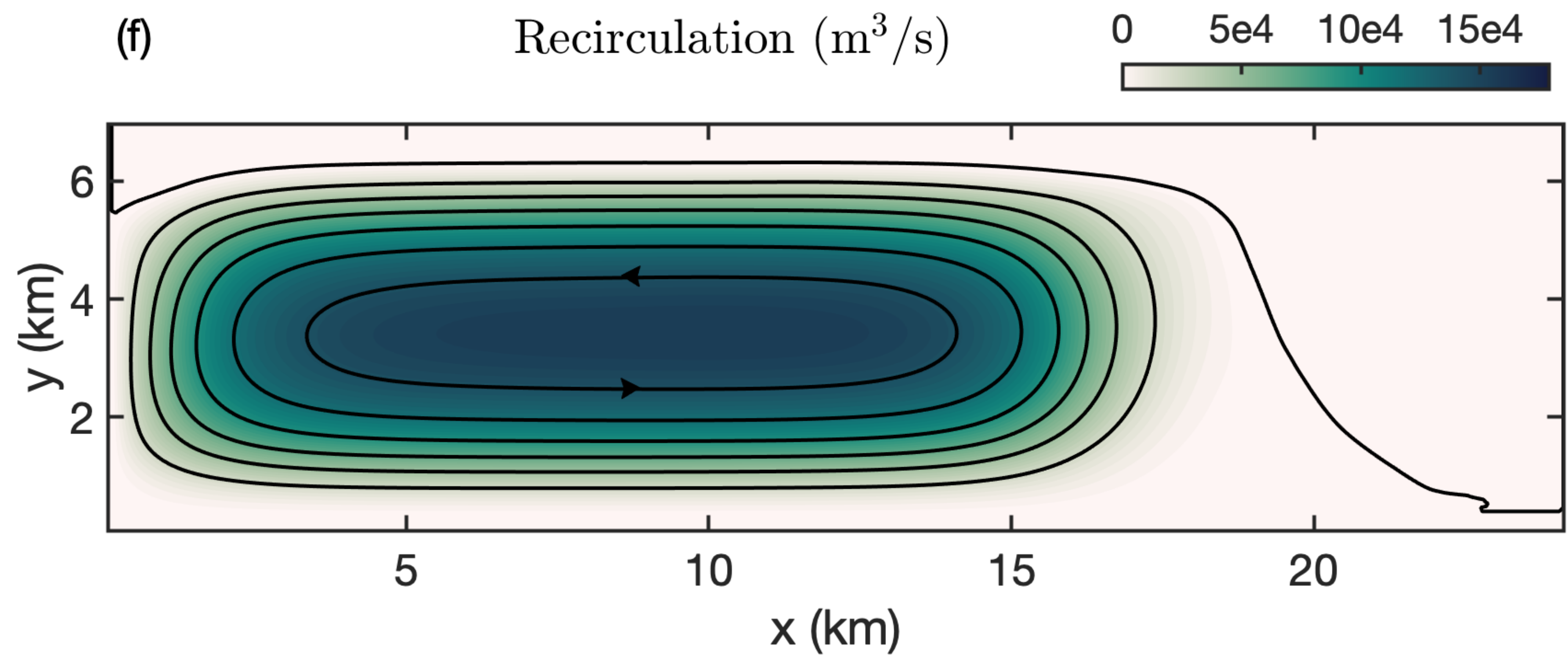
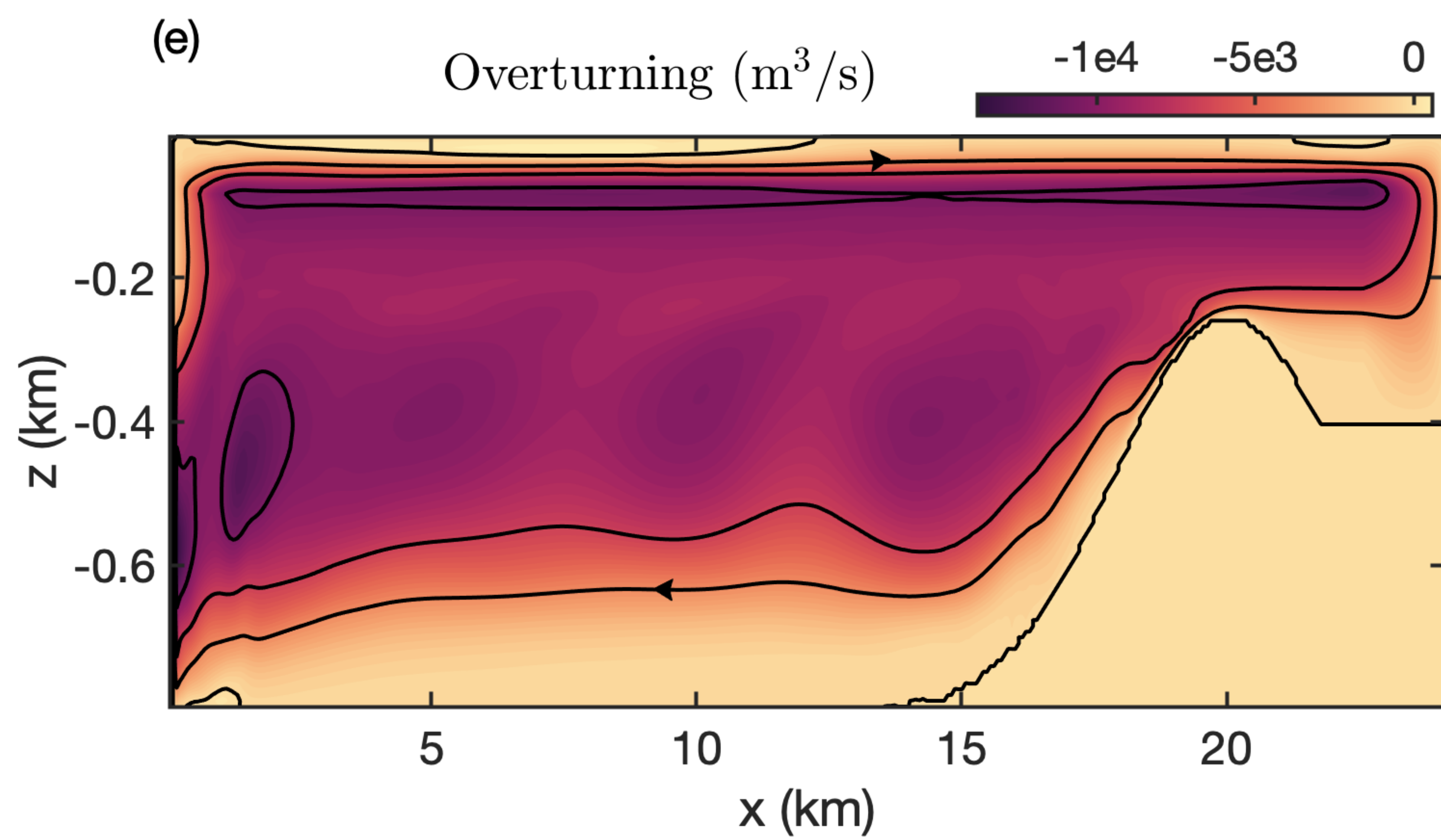
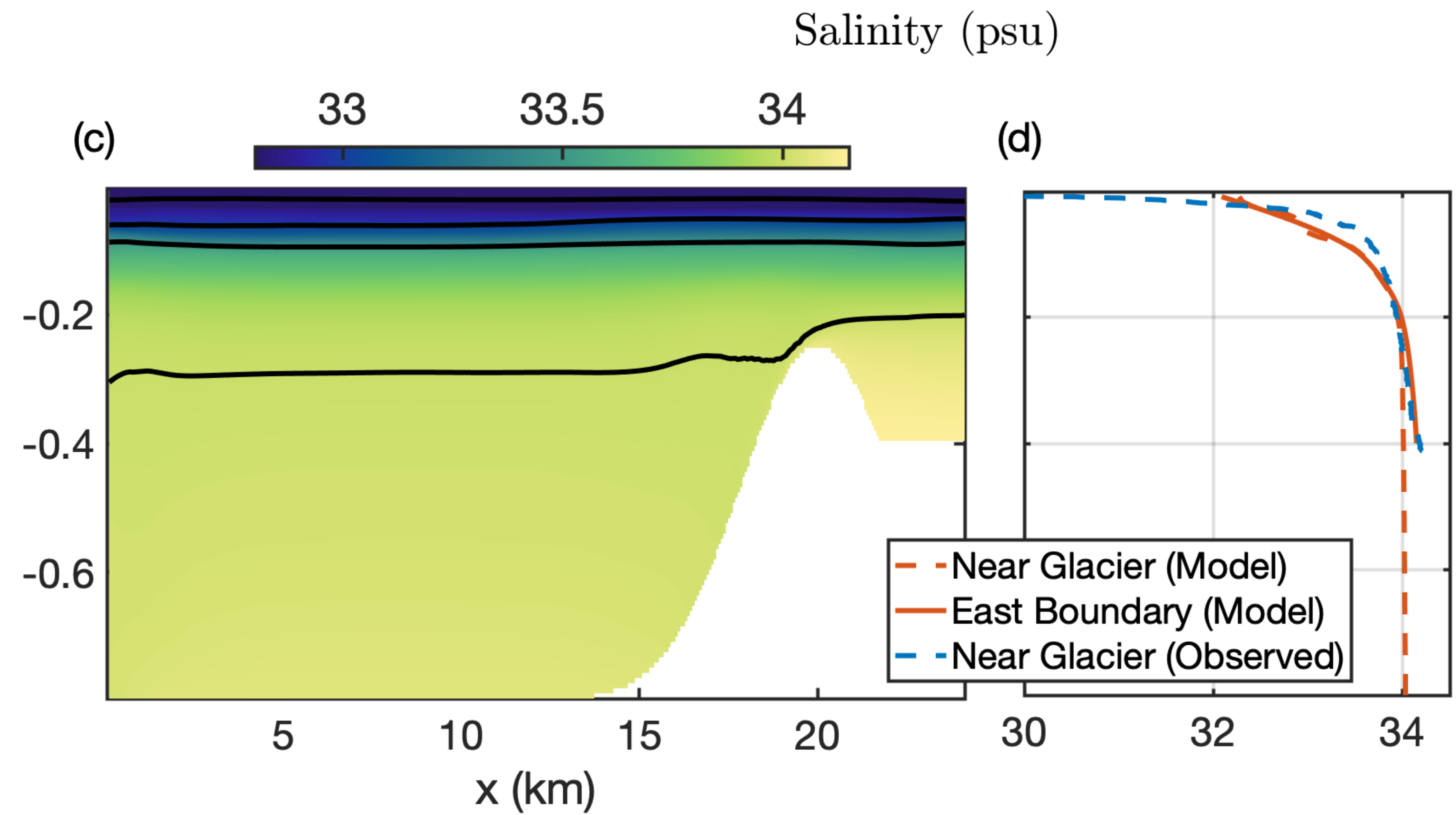
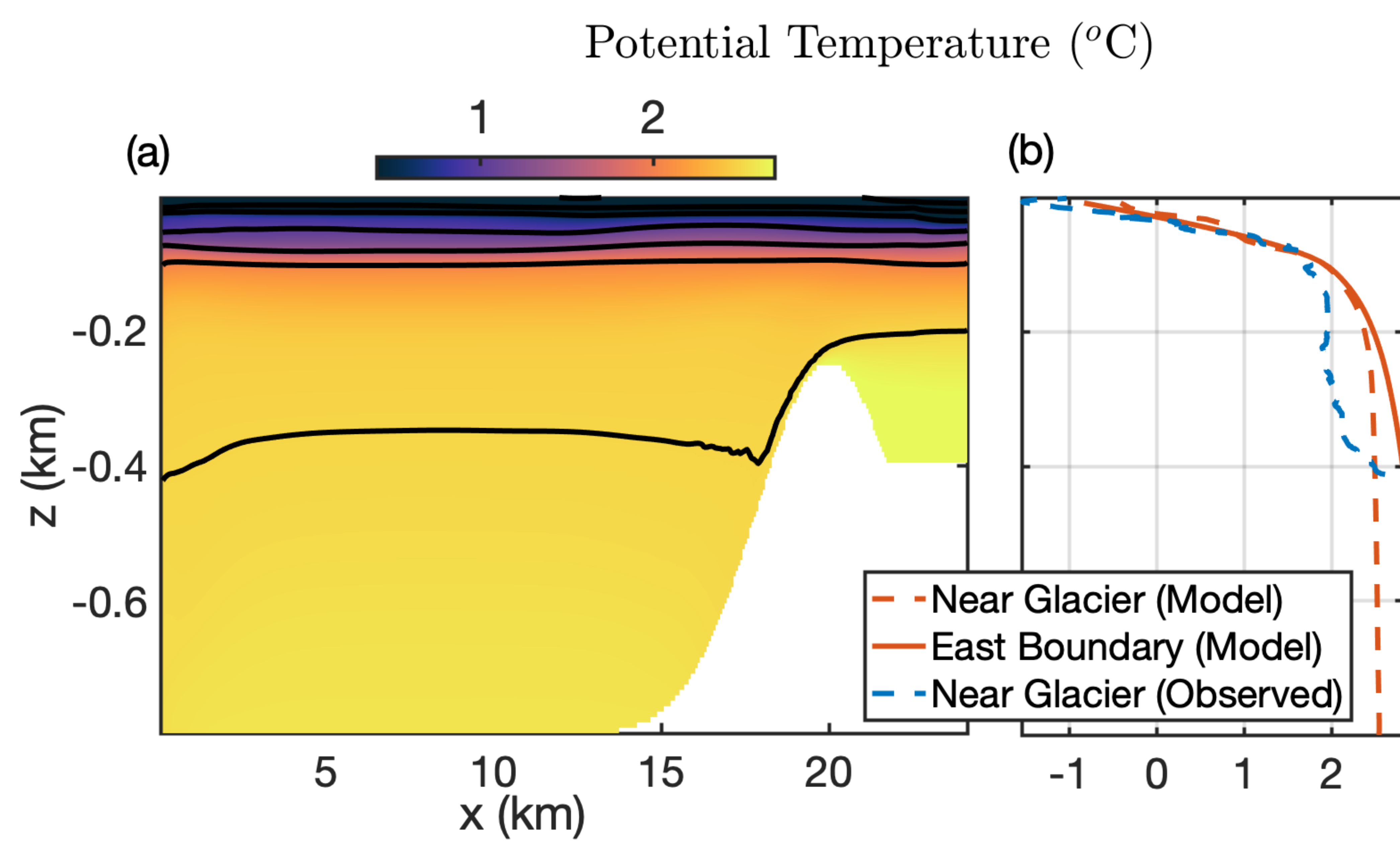
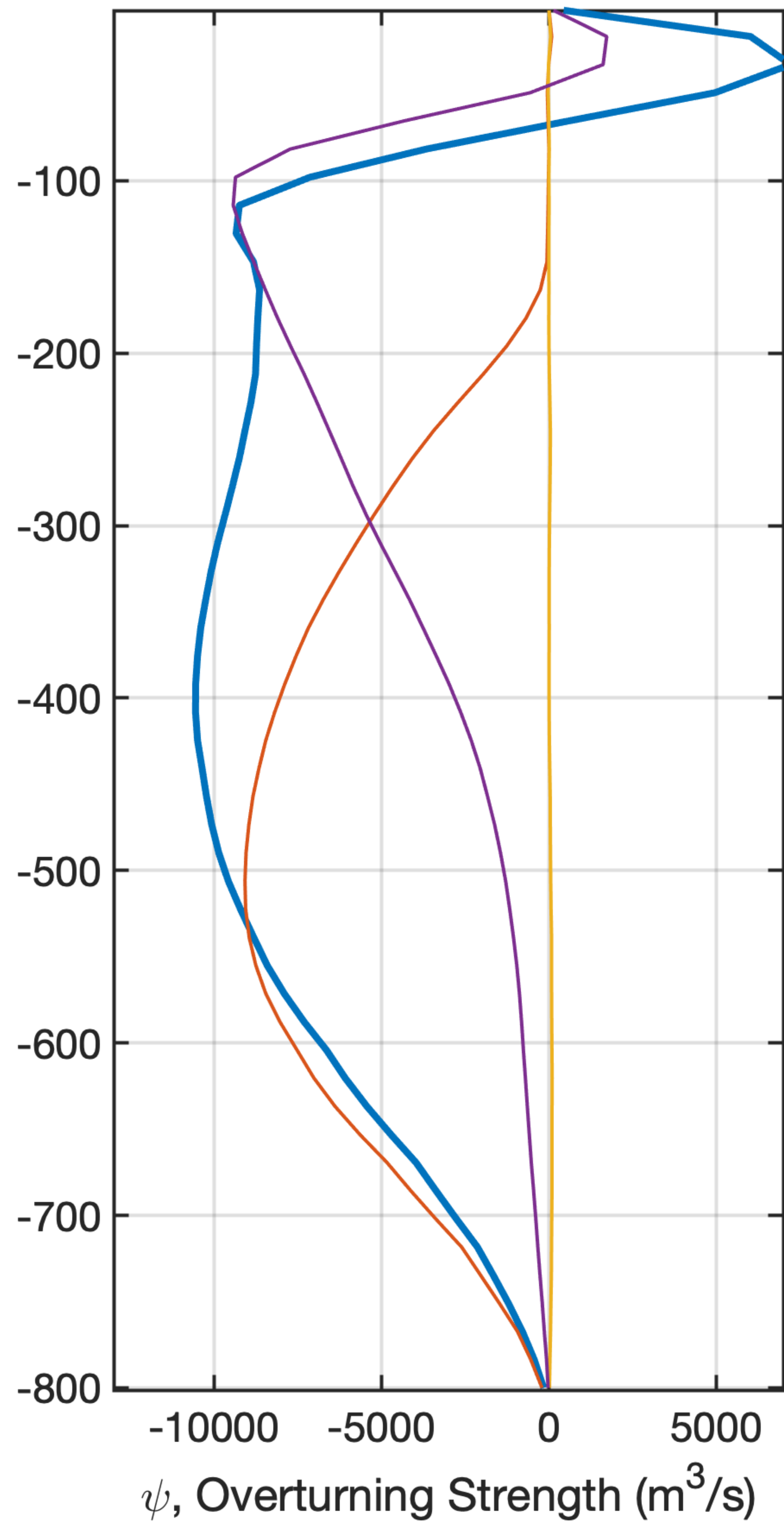
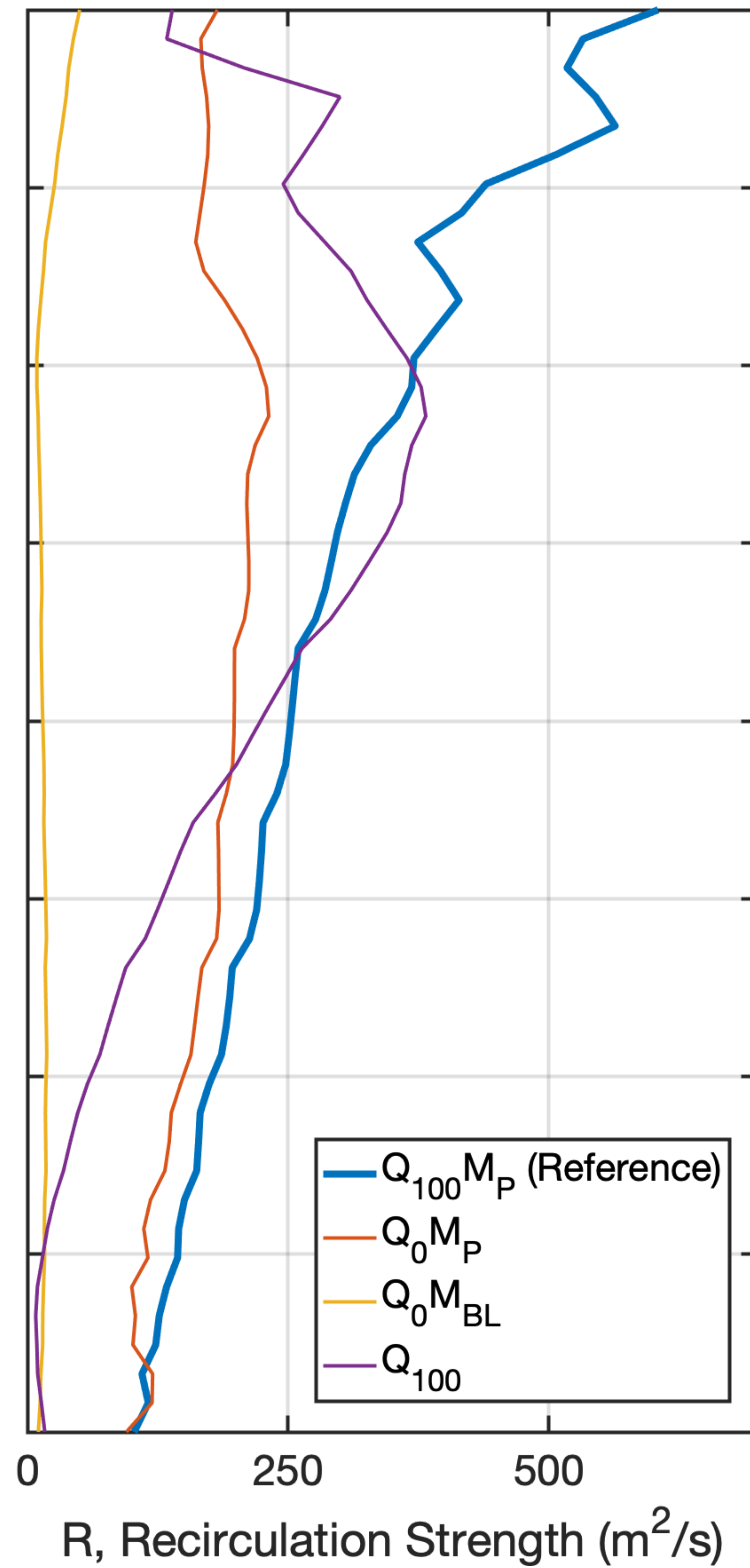
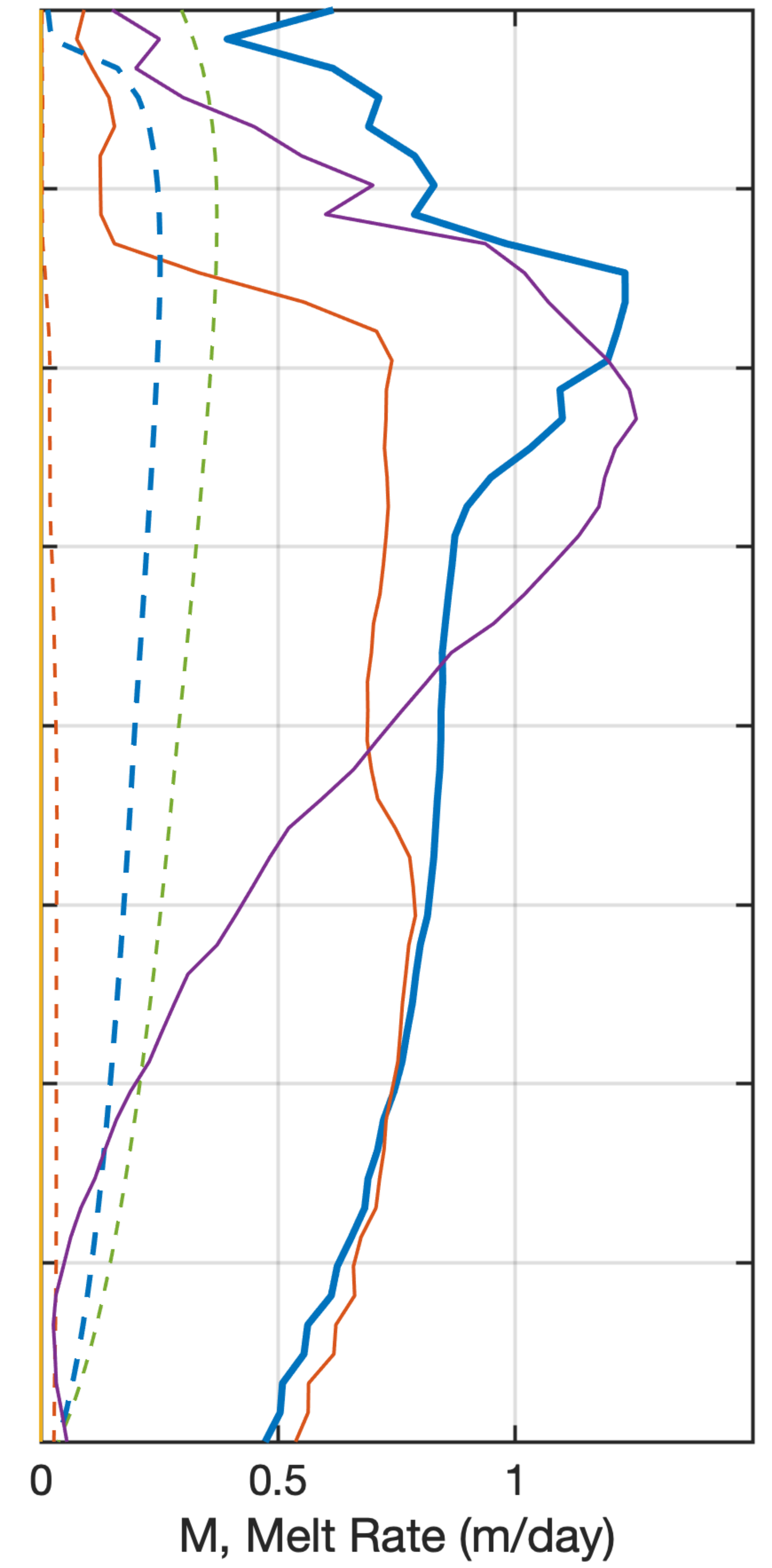


Figure 3.

(a)**(b)****(c)**

— $Q_{100} M_P$ (Reference)
— $Q_0 M_P$
— $Q_0 M_{BL}$
— Q_{100}

Figure 4.

